PHOTONICS Research

All-fiber-optic mass sensor based on optomechanical nanofilm resonators

Qiao Lin,[1] Xin Ding,[1] Weiguan Zhang,[2] Yueliang Xiao,[1] Mingxiu Wang,[1] Jingyi Hou,[1] Congmin Li,[1] Chenxu Li,[1] Changrui Liao,[1,3] Yiping Wang,[1,2] and Shen Liu[1,*]

[1]Shenzhen Key Laboratory of Photonic Devices and Sensing Systems for Internet of Things, Guangdong and Hong Kong Joint Research Centre for Optical Fibre Sensors, State Key Laboratory of Radio Frequency Heterogeneous Integration, Shenzhen University, Shenzhen 518060, China
[2]Guangdong Laboratory of Artificial Intelligence and Digital Economy (SZ), Shenzhen 518107, China
[3]Shenzhen Key Laboratory of Ultrafast Laser Micro/Nano Manufacturing, Key Laboratory of Optoelectronic Devices and Systems of Ministry of Education/Guangdong Province, College of Physics and Optoelectronic Engineering, Shenzhen University, Shenzhen 518060, China
*Corresponding author: shenliu@szu.edu.cn

Received 4 November 2024; revised 28 February 2025; accepted 19 March 2025; posted 20 March 2025 (Doc. ID 546219); published 27 May 2025

Mass detection plays an indispensable role in many fields like medical targeted therapy, biological cytology, and nanophysics. However, traditional mass detection faces the challenge of a complex system, expensive instruments, and long testing time. Here we report an all-fiber-optic mass sensor based on a nanofilm resonator. Using resonant frequency shifts as the readout of analyte mass, the sensor achieves the mass sensitivity of 0.920 kHz/pg with a mass resolution of 1.9×10^{-14} g, for the first-order mode in the mass range up to 372 pg at room temperature. In this work, we transfer the excitation laser and detection laser to the micro-cavity structure at the end of the optical fiber. Combined with optical fibers, the sensor can be made extremely integrated, making it more stable and collimation-free compared with traditional bulky optical setups. Its good biocompatibility and anti-electromagnetism disturbance ability also make this mass sensor potentially a beneficial tool for cell biology and basic physics measurements.

https://doi.org/10.1364/PRJ.546219

1. INTRODUCTION

Mass detection is critical in many disciplines such as chemical science [1], cell biology [2,3], and nanoelectronics [4]. For example, in targeted drug delivery and tumor imaging applications, precisely adjusting the dose of metal nanoparticles can directly improve the therapeutic effect [5]. The common mass measurements are generally based on mass spectrometry, cavity optomechanics [5–7], gas chromatography, and so on. Among them, mass spectrometry, with a very high accuracy, is used to detect charged analytes by means of dissociation [8,9]. However, when measuring heavier species such as nanostructures and biological components, the charged analytes are successively fragmented by several dissociation methods causing complex mass spectrum patterns, which greatly reduces the performance [5]. The cavity optomechanical effect uses an optical resonator to couple the optical mode with the mechanical vibration mode. Through the vibration of the nanomechanical resonator, weak dynamic signals such as micro-mass changes can be converted into the modulation of the optical mode. This provides another simple and effective alternative optical measurement to compensate for the limitations of traditional mass spectrometry. Utilizing optical readout, we can realize the real-time monitoring of weak dynamic signals, such as weak pressure [10,11], small mass [6], thermal radiation [12,13], weak current [14], and trace gas [15]. In 2016, Malvar *et al.* [5] measured the mass of gold nanoparticles and *Escherichia coli* by monitoring the resonant frequency of a silicon nitride cantilever beam. Since deconvolution of mass and adsorption location can be obtained by measuring at least two vibration modes, the group also measured high-order vibration modes of the cantilever beam to analyze the particle position. Some higher-order modes typically resonate at very high frequencies, showing advantages in achieving high resolution and fast response [12,15,16]. Moreover, in 2021, Stassi *et al.* [17] utilized a two-photon polymerization technique to print NEMS resonators with quality factors up to 15,000 and mass sensitivity of 450 zg. This combination of cavity mechanics and extreme miniaturization in NEMS offers the possibility to reach an unprecedented resolution in high-performance mass sensing.

Cavity optomechanical resonators can be categorized into electronic and optical drives based on their actuation methods, each with distinct pros and cons. Electronic drive typically employs a PZT [5] or an additional conductive layer on the resonator surface, combined with an electric current to generate force [13]. This actuation method is straightforward in terms of principle and operation. Compared to the complex optical path

system of traditional optical drives, it features simpler equipment and a more robust system. However, due to the presence of PZT, the probe's overall size cannot be significantly reduced, even if the sensing head is a nanoscale mechanical resonator, which hinders integration. Moreover, the electronically driven probe remains an active device, susceptible to electromagnetic interference and not resistant to electrochemical corrosion, limiting its application in complex and confined environments. In contrast, optically driven optomechanical resonators can reduce parasitic capacitance and thermal-mechanical displacement noise, and operate non-invasively. Therefore, simplifying the traditional bulky optical drive system and integrating it into a compact surface could harness the benefits of optical actuation while avoiding the drawbacks of electronic drives.

In recent years, the development of sensors based on fiber-end microstructures has offered an excellent solution to the aforementioned challenge. Common fiber-end microstructure sensors include those based on a Fabry-Perot interferometer (FPI) [18–21], small-size tip lenses [22–24], and microbubble cavities [25]. Among these, sensors based on FPI are of significant research interest due to their simple principles, flexible design, and stable structure. However, the commonly used wavelength demodulation is generally fit for static measurements, but inadequate for precise large dynamic signal assessment. And it is also constrained by the spectrometer resolution and the free spectral range. Although research into optical fiber applications for mass sensing is sparse, with limited studies at the gram level, we have also noted the outstanding work by Yu *et al.* [26] recently, who bent a micro-nano fiber into a U-shape to create a cantilever beam and used a gold microflake as a sample tray to form a microbalance, enabling the measurement of tiny particles in the range of 0 to 15 ng. Inspired by such researches, we believe that combining the fiber platform with nanomechanical resonant cavities could provide a new approach for developing novel mass sensors.

In this work, a hollow core fiber (HCF) is spliced to the end face of single-mode fiber to support and suspend a trampoline-type graphene nanofilm resonator, forming a highly integrated all-fiber open FPI for mass sensing. Analytes land on the nanomechanical resonator via a magnetron sputtering system in a low vacuum of 2 Pa. The shifts of resonant frequencies serve as the readout of mass. At room temperature, the sensor exhibits mass sensitivities of –0.920 kHz/pg and 2.010 kHz/pg for the first and second order modes, respectively, with a mass range up to 372 pg. The mass resolution of 1.9×10^{-14} g is calculated. Traditional mass measurement like mass spectrometry tends to significantly reduce its performance when detecting heavier substances such as nanostructures and biological components. Its application is generally limited to light analytes ($<10^{-19}$ g). Here, the mass measurement that we proposed offers a complementary approach in the picogram range for the field of mass sensing. In the measurement configuration, a sine-sweep modulated laser and another single-wavelength laser with a narrow linewidth are transmitted through the fiber to drive and detect the mechanical vibration of the resonator, respectively. This method effectively simplifies the previously complex and bulky optically driven system, achieving integration and enhanced stability without the need for collimation. What is more, as a flexible sensor, fiber exhibits excellent bending properties as well as its superior biocompatibility and anti-electromagnetic interference characteristics, which make this mass sensor promising for detection in complex and multi-curved environments.

2. EXPERIMENTAL METHOD

A. Sensing Principle

The nanomechanical mass sensor fabricated in this study is illustrated in Fig. 1. This device senses external physical quantities by forming an optical resonator at the tip of an optical fiber, utilizing the vibrations of the nanomechanical resonator. The optical resonator is a Fabry-Perot cavity composed of two reflective surfaces: a fixed single-mode fiber end face and a multilayer graphene film (MLG) supported by HCF. Under the excitation of periodic external forces, such as dynamically varying air pressure or optical forces, the MLG film can undergo forced vibrations, acting as a harmonic oscillator. Since the resonant frequency of the resonator is related to its mass, it satisfies the following equation [27]:

$$f_m = \frac{1}{2\pi}\sqrt{\frac{k}{m_{\text{eff}}}}, \tag{1}$$

where k represents the elastic coefficient. When the change in the mass of the resonator is Δm_{eff}, the drift in the resonant frequency is Δf_m. Thus, the relationship between the mass increment of the resonator and the drift in the resonant frequency is given by

$$\Delta m_{\text{eff}} = 2m_{\text{eff}}\Delta f_m / f_m. \tag{2}$$

Therefore, by monitoring the variation in the resonant frequency, it is possible to detect the added mass on the resonator, with the change in the film's mass being linearly related to the change in the resonant frequency.

Additionally, for a film undergoing forced vibrations, the in-plane stress of the film will undergo periodic changes when a beam of light at a certain frequency is applied to the film. In this

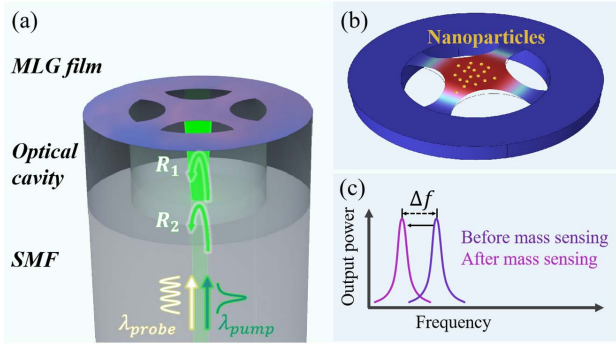

Fig. 1. (a) The scheme of the optomechanical mass sensor. (b) The scheme of analytes acting on graphene membrane. (c) Detection of mass-induced tension increases by monitoring the resonant frequency of the optomechanical resonator.

case, the resonant frequency of the film can also be calculated using the following equation [27]:

$$f_m = \frac{\alpha_{mn}}{2\pi}\sqrt{\frac{S}{\rho t}}, \tag{3}$$

where α_{mn} is a constant related to the vibration mode order, with subscripts (m, n) representing the number of nodal diameters and nod circles, respectively. The constant α_{mn} varies according to different orders modes (m, n) of the film vibration, for example, $\alpha_{01} = 2.404$, $\alpha_{11} = 3.832$, $\alpha_{21} = 35{,}135$. ρ denotes the surface density of the film. S is the total tension of the film, and t represents the thickness of the film. For a composite film with a thickness of t, changes in t lead to a corresponding drift in f_m. Combined with Eq. (3), for the same resonator, its resonant frequency f_m decreases as the thickness t of the composite film increases. Using Eq. (3), it is therefore possible to measure small masses by detecting changes in the resonant frequency.

B. Sensor Fabrication and Characterization

Figure 1(a) illustrates the schematic diagram of the proposed optomechanical mass sensor. Its fabrication process mainly consists of two steps. First, as shown in Fig. 2(b), a single-mode fiber is spliced with an HCF, whose inner diameter is 75 μm, using a splicing machine. Then the end of the HCF is cut flat with a cutting knife. Meanwhile the length of the HCF, which serves as the initial cavity length of the Fabry-Perot interferometer (FPI), is controlled and monitored in real-time through a microscope. The length here is measured as 54 μm under the microscope. Following this, the MLG film is transferred to the open micro-cavity end of the fiber and suspended using the graphene wet transfer technique [28]. Figure 2(a) shows a Raman spectrum of the suspended graphene on the end face of the resonator, whose scanning electron microscope (SEM) image also is shown in the inset. Unlike a traditional drum head resonator, we utilize a focused ion beam (FIB) etching method to create four circular holes on the suspended graphene film, with the centers of the circles located on the concentric circle of the MLG film. Each circle is rotated around the center of the graphene film by an interval of 90° to form a trampoline-shaped membrane, resulting in a trampoline-type fiber end face resonant structure. The SEM image of this structure is shown in Fig. 2(c). Achieved by selectively trimming sections from a conventional drum head membrane resonator, this suspended trampoline structure allows for the release of some tension, thus obtaining a low-tension suspension structure that enhances the mechanical quality factor (Q-factor) and reduces the damping coefficient. Furthermore, the non-linear machining process also makes the film less prone to damage during fabrication and operation. Studies have indicated that such shaped trimming can improve the reproducibility of device fabrication in terms of the resonant frequency and mechanical sensitivity [15].

C. Mass Measurement

As shown in Fig. 3(a), the mass detection system based on the cavity optomechanical effect constructed in this study utilizes two tunable single-wavelength lasers. One serves as the excitation light source with a wavelength of λ_1, and the other as the detection light source with a wavelength of λ_2. The laser generated by Laser A is modulated by an electro-optic modulator (EOM) and then sequentially passes through a 90:10 fiber coupler and a circulator before entering the optical fiber graphene film resonator. The laser from Laser B enters the optical fiber graphene film resonator through the other port of the 90:10 fiber coupler and the circulator. The phase difference between the reflected light from the fiber end face and that from the graphene film will change with the surface tension of the graphene film. The reflected light is returned through the circulator and detected by a photodetector (PD), with its spectral signals displayed by a vector network analyzer (VNA). In particular, in order to eliminate the influence of the excitation light on the demodulated signal (detection light signal), a tunable band-pass filter is used to filter out the excitation light. Additionally, a periodic signal generated by a signal generator is used as the RF signal for the EOM. As shown in Fig. 3(b), the device is connected to a spectrometer and a broadband light source via the circulator for spectral

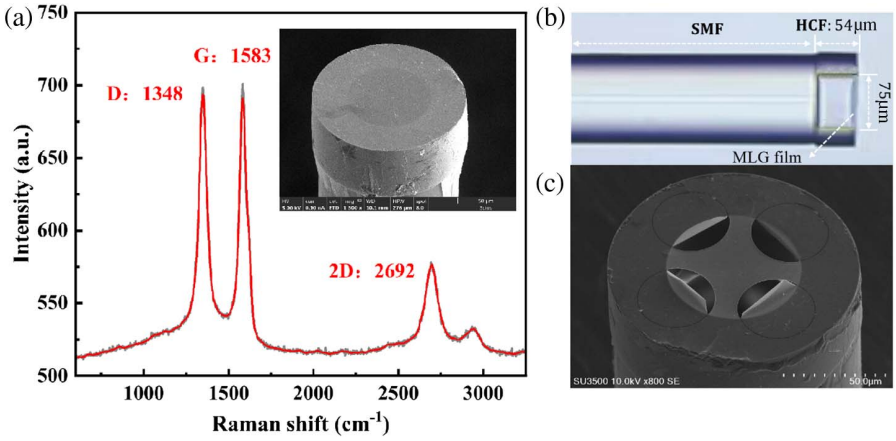

Fig. 2. (a) Raman spectrum from the suspended multilayer graphene film measured by a 532 nm laser. The inset shows the SEM image of the resonator before etching. (b) The side view of the open optical cavity at the fiber end face under the microscope. (c) The SEM image of the trampoline-type resonant structure covering the fiber end facet.

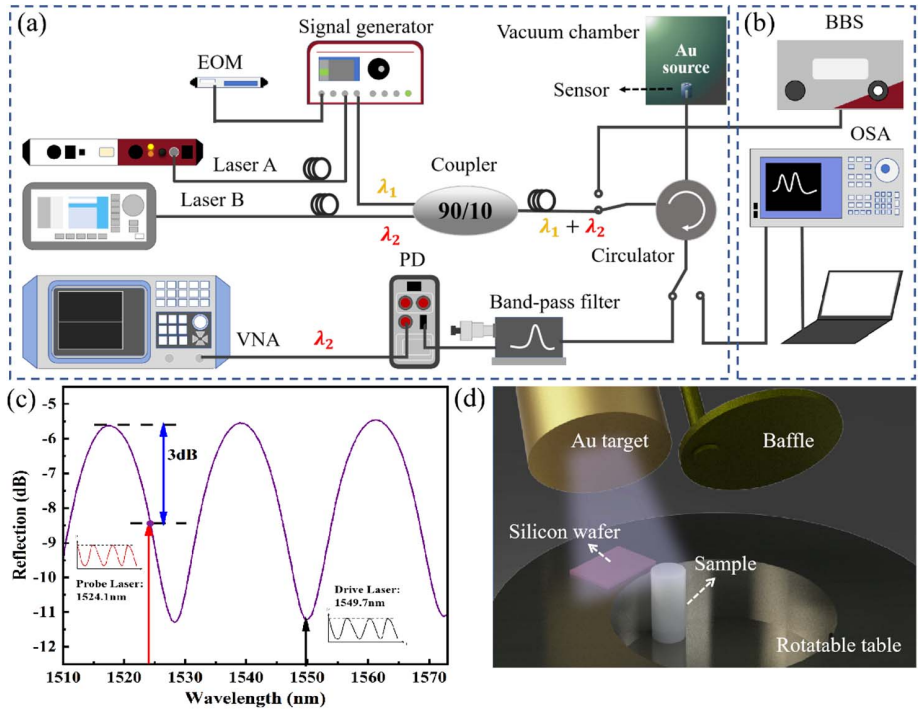

Fig. 3. Experimental setup. (a) The optical excitation and detection system used to monitor the response of the fiber tip resonator to change in Au mass. (b) The apparatus used to acquire optical reflection spectra. EOM, electro-optic modular; VNA, vector network analyzer; PD, photodetector; BBS, broadband light source; OSA, optical-spectrum analyzer. (c) The reflection spectrum of trampoline-type graphene film resonator. (d) The device of the mass source supplied by the Au target.

testing and its reflection spectrum is shown in Fig. 3(c), with a contrast ratio of about 6 dB and an $FSR_{(m,m-1)}$ of 22 nm. $FSR_{(m,m-1)}$ here is the free spectral range of the interference spectrum. On this basis, the length of the Fabry-Perot cavity, L_{FP}, can be calculated according to the equation [29] $L_{FP} = \frac{\lambda_m \lambda_{m-1}}{2 n_{eff} FSR_{(m,m-1)}}$, where λ_m is the resonant wavelength of the mth order interference dip/peak and n_{eff} is the effective index of the intracavity medium. The calculated cavity length is approximately 53.83 μm. Based on dynamic signal demodulation principles, the wavelength at the maximum slope (orthogonal working point, that is, 3 dB) is selected for optical detection. Therefore, the wavelength of detection light is set to 1524.1 nm, with its optical power being set to 6.5 mW. The wavelength of excitation light is chosen to be 1549.7 nm. During the experimental test, the power and wavelength of excitation and detection light are kept unchanged. Lastly, the mass source here, as shown in Fig. 3(d), is supplied by the Au target, with the sensor and silicon wafer placed under it.

3. RESULTS AND DISCUSSION

A. Optomechanical Frequency Response

Here, the resonant frequency of the resonator is analyzed and simulated by the finite element method utilizing the solid mechanics and thin film modules of COMSOL Multiphysics. The insets in Fig. 4(a) display the simulation results for the mechanical vibration modes of the first and second order resonance frequencies, especially the flapping and tilting modes. Then we use a vector network analyzer to measure the first and

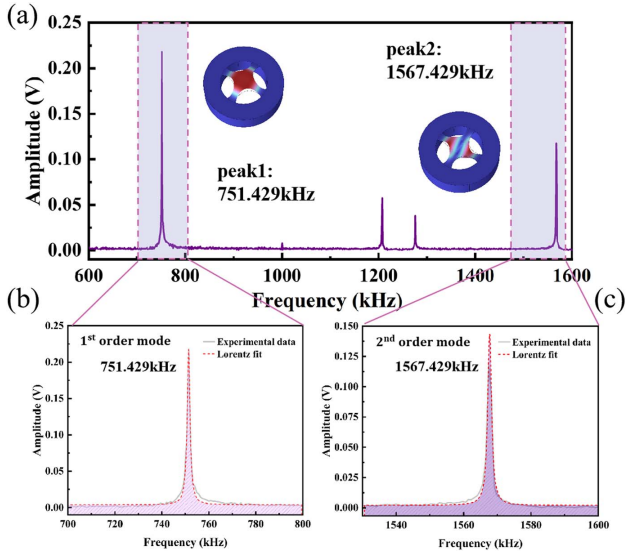

Fig. 4. (a) Mechanical frequency characteristics of the sensor. Insets: the simulation of the first and second order modes of the resonator obtained through finite element method. (b), (c) Amplitude versus frequency plot of the resonator. The dotted lines are Lorentz fitting of two resonance peaks in linear coordinates.

second order resonance frequencies of the resonator, corresponding to the (0,1) and (1,1) modes. The peak frequencies are observed at 751.429 kHz and 1567.429 kHz, respectively.

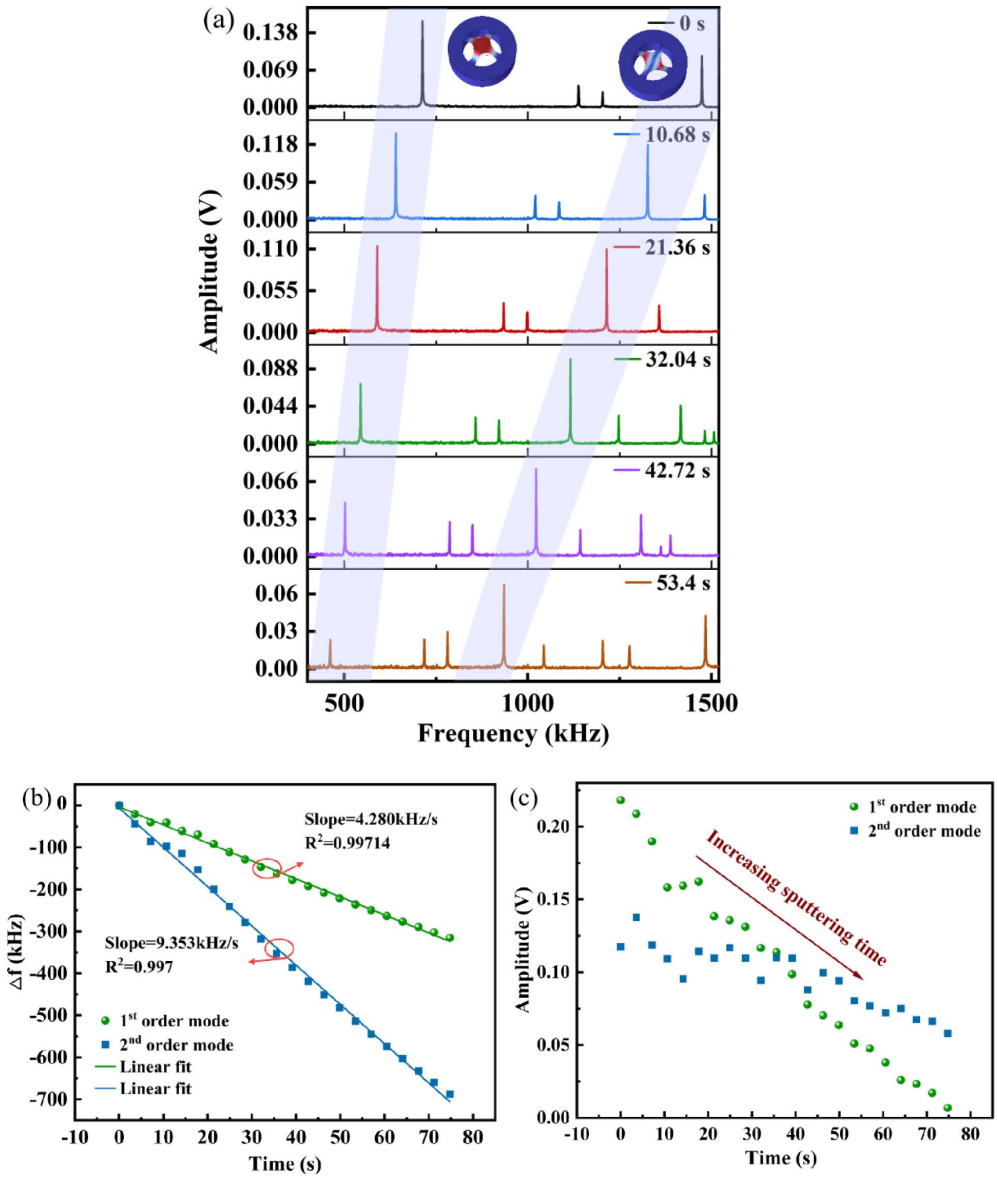

Fig. 5. Mass sensing results. (a) Frequency characteristics of the first and second order modes of the resonator as functions of time in response to increasing masses during the sputtering process. (b), (c) Plotted results of peak searching of (a), showing shifts of resonant frequencies and variation of amplitude at these two frequencies, respectively.

Figures 4(b) and 4(c) show that the amplitude responses for both the first and second order modes closely align with Lorentzian fits, which is consistent with the behavior of a linear damping oscillator. This agreement also reflects the effective decoupling of optical driving and detection.

B. Sensing Results

The corresponding mass sensing results are shown in Fig. 5. It illustrates the evolution of the frequency spectrum of the graphene film as gold deposition time increased. The vector network analyzer is controlled by MATLAB to perform automatic scanning, allowing time-monitoring of the resonator's resonant behavior. Data are recorded every 3.56 s over a total duration of 80 s. More specifically, from Fig. 5(a), it can be observed that both the first and second order resonance peaks exhibit an obvious shift towards lower frequencies along with increasing gold mass. To characterize the relationship between the peak resonant frequency and the increase in gold mass more clearly, the plot of the peak frequency versus the deposition time is shown in Fig. 5(b). From the data, the sensitivity value of the sensor is calculated to be 4.280 kHz/s and 9.353 kHz/s for the first and second resonant modes based on linear fits, respectively. The higher-order resonant modes exhibited greater sensitivity within the same mass range, suggesting that the device's sensitivity could be enhanced by observing higher-order modes. Additionally, from Fig. 5(c), it is clearly demonstrated that the amplitude values of the resonance peaks decrease gradually with the increasing gold mass. This phenomenon may be attributed to the influence of gold film thickness on the built-in stress of the graphene film. When light energy

is applied to the composite film, a thicker film requires more light energy to convert into mechanical energy to achieve the same vibration. Therefore, under identical optical power excitation, thicker films display lower amplitudes, leading to a certain measurement limit for the device. Notably, the amplitude values exhibit fluctuations in decline, which could be due to the limited number of data points collected and resolution of the analyzer. Also, since the deposition of gold particles requires some time, the deposition duration varies depending on particle size and location, leading to uneven thickness distribution in the gold film. Consequently, the amplitudes obtained from real-time monitoring display fluctuations. This result also indirectly validates the rationale that monitoring resonant frequencies is a more reasonable and stable method for indirectly measuring minuscule masses compared to amplitude changes. The variation in amplitude for the second order resonance peak is smaller than that of the first order peak, which could be attributed to the inherently smaller magnitude of the second order resonance peak, making it less sensitive to micro-mass changes.

C. Calibration

In this paper, the mass generation and control system is a magnetron sputtering system. Metal nanoparticles serving as analytes are supplied by magnetron sputtering, where an electron beam is accelerated to impact the target surface under an applied electric field. According to the principle of momentum conservation, metal nanoparticles on the target surface are ejected with a certain velocity, which allows them to deposit onto the surface of the graphene film resonator. By adjusting the voltage and current parameters of the magnetron sputtering system, the electron velocity can be controlled, thereby adjusting the deposited mass of nanoparticles on the graphene surface. In this paper, the Au target as shown in Fig. 3(d) is chosen as the mass source due to its good ductility and consistent film formation. In order to observe the change of resonant frequency with mass clearly, minuscule mass detection is realized by calibrating the mass of Au-plated film in the experiment. The baffle above the coating of the vacuum chamber is closed, and the graphene film resonator is fixed directly below the baffle, so that only a small number of Au atoms are allowed to deposit on the surface of the graphene film resonator. Simultaneously, a clean silicon wafer is fixed at the fixed position of the graphene film resonator for calibrating the gold mass.

Here, the added mass of Au is calculated by multiplying the density of Au by its volume. The area of the trampoline-type graphene film resonator is calculated by using a mathematical model. The thickness of the Au film is measured using atomic force microscopy (AFM). Prior to AFM testing, the silicon wafer surface is lightly scratched with tweezers to artificially introduce a measurable height difference in the film. AFM is then used to observe the morphology of the Au film on the silicon wafer and measure the thickness of the Au film at different locations (along the start and middle of the scratch) [Fig. 6(a)]. The measuring result is demonstrated in Fig. 6(b). From the inset, it can be observed that the Au film is uniformly distributed on the silicon wafer surface, with a noticeable height difference at the scratch area. AFM results show that the thicknesses of the Au film measured at different positions near the sensor are 19.785 nm, 17.548 nm, 16.642 nm, 16.587 nm, 16.237 nm, and 16.201 nm. The thickness variation of different positions at the same wafer is minor, attributed to the circular shape of the deposition mask, where the Au film is thicker near the outer edge. Since the graphene film is placed inside the deposition chamber, the average thickness of the Au film measured from the middle and inner positions of the silicon wafer is taken as 17.176 nm. Consequently, the detection range of mass is up to 372 pg. In Fig. 7, we combine this with results from Fig. 5(b) with linearity close to 99% and the sensitivity of the resonator is 0.920 kHz/pg and 2.010 kHz/pg, for the first and second order modes, respectively. Furthermore, the detection limit (DL) can be calculated according to the equation that is introduced by White *et al.* [30] as

$$\mathrm{DL} = \frac{3 \cdot \delta}{S}, \tag{4}$$

where δ and S respectively represent the individual noise variance and mass-detection sensitivity. We analyze the background frequency spectrum after testing for the δ evaluation, which is calculated as 0.072 kHz using standard derivation analysis [31]. Hence, a mass detection limit is obtained as

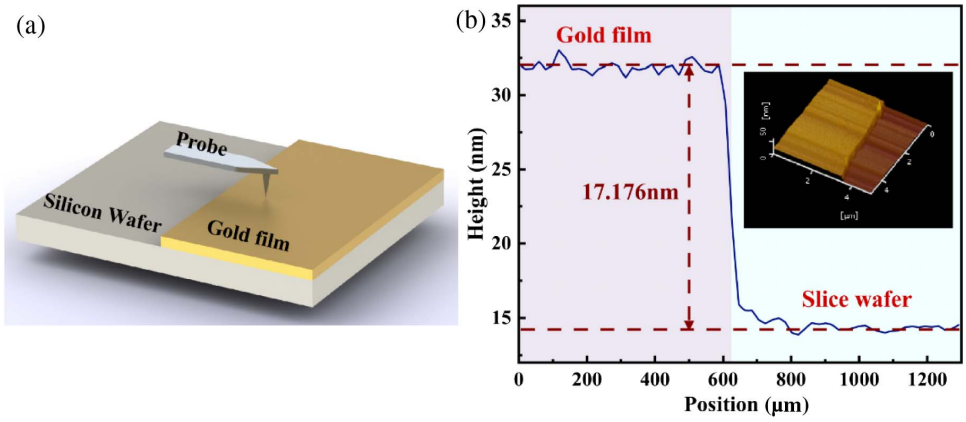

Fig. 6. (a) The diagram of the silicon wafer used to measure the thickness of the added Au film. (b) The calibration result of the thickness of Au film measured using atomic force microscopy (AFM).

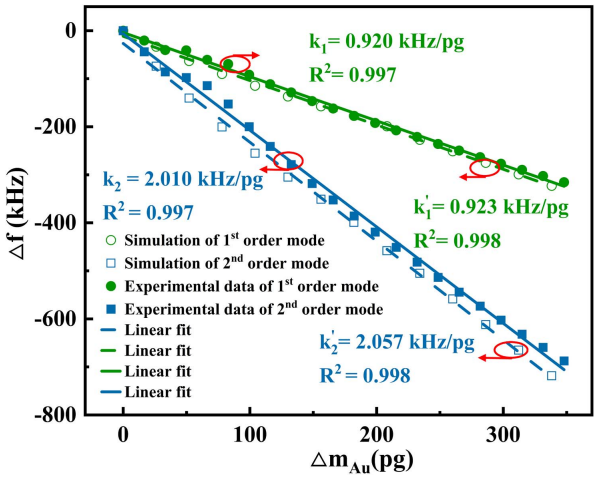

Fig. 7. Shifts of resonant frequencies in response to increasing masses in comparison with predictions of the simulation model. k_1, k_1', k_2, k_2' represent the slope of linear fits. R^2 denotes the linearity of the fitting result.

2.35×10^{-14} g. Lastly, we also employ finite element analysis using COMSOL software to simulate the response of a graphene film on the tip of an optical fiber to gold mass. Specifically, we perform a parametric scan to simulate the impact of different gold thicknesses on resonant frequencies. As shown in Fig. 7, the experimental results are consistent with the prediction in simulation.

D. Stability of System

During the mass testing, the graphene film resonator is put in the vacuum chamber of the magnetron sputtering deposition system. Fluctuations in the chamber pressure can affect the resonant frequency of the resonator. Therefore, this study also evaluates the system stability by monitoring changes in the fundamental resonant frequency of this optomechanical resonator [10].

First, the stability of the system is assessed prior to the mass testing experiments. During the testing process, all devices in the system are kept in fixed positions with constant parameters. The period is 20 min, during which a set is collected every 10 s. The plotted results of peak searching of the resonator's frequency spectrum over time are shown in Fig. 8. It can be observed from the figure that the frequency spectrum of the resonator remains generally constant over 20 min, indicating that the environment within the vacuum chamber is stable. The fluctuation range of the resonator's resonant frequency is approximately 0.03 kHz, displaying random fluctuations. These fluctuations may be related to the resolution bandwidth of the spectrum analyzer and the testing frequency, confirming that the system's stability is good. After the mass sensing test is completed, the system's stability is re-evaluated in the same way. During the 20 min period, the resonant frequency drifted approximately 0.25 kHz. This behavior may be attributed to the optical heating accumulation effect, or preheating. The frequency measurement error could be characterized using Allan deviation, defined as [13]

$$\sigma_A = \frac{1}{f}\sqrt{\frac{1}{2(N-1)}\sum_{j=2}^{N}(f_j - f_{j-1})^2}, \tag{5}$$

where f_j is the resonant frequency extracted at the measurement in Fig. 8. The Allan deviation is calculated as 2.97×10^{-5}. Thus, a mass resolution δm of 1.90×10^{-14} g is obtained by using the equation $\delta m = \frac{\delta f}{\text{sensitivity}} = \frac{\sigma_A \times f_0}{\text{sensitivity}}$, where the sensitivity is the first order mode in kHz/pg and δf corresponding to the above equation here is the intrinsic inaccuracy in the resonant frequency determination [10].

4. CONCLUSION

In conclusion, we demonstrate that mass sensing based on resonant frequency tracking of vibration modes with optical excitation is a suitable approach for precise mass detection. In contrast with traditional mass sensors, our device exhibits a resolution as small as 1.90×10^{-14} g and great stability in mass sensing for nanosized analytes, which opens the door to relevant biomedical applications. Utilizing the principle of cavity optomechanics, the added mass response sensitivity of this optomechanical resonator is determined to be 0.920 kHz/pg and 2.010 kHz/pg for the first and second order modes, respectively, with the added mass range up to 372 pg at room temperature. This result confirms that a higher-order mode of the

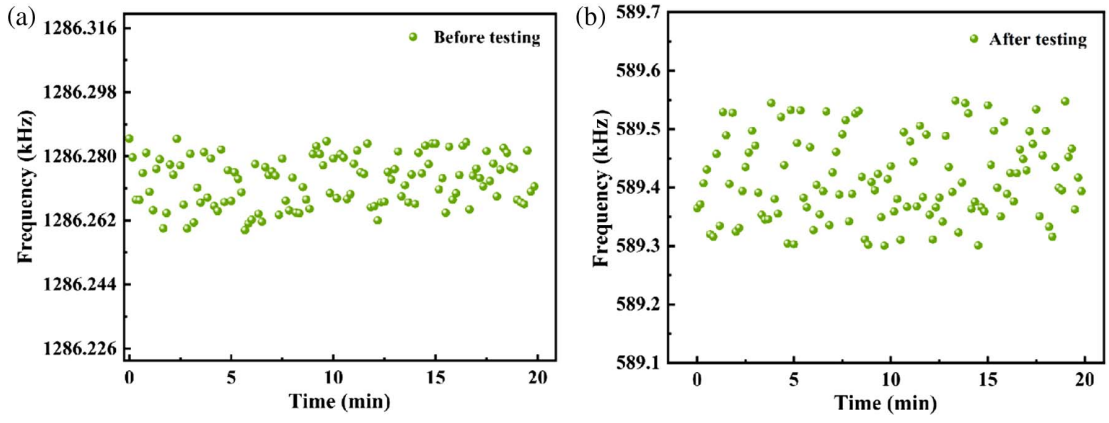

Fig. 8. Experimental assessments of frequency stability. (a) Frequency stability before testing. (b) Frequency stability after testing.

resonator provides better mass sensitivity in the same sensing range with the same general trends. Therefore, enhancing mass sensitivity could potentially be achieved by observing higher-order modes. Finally, this all-optical sensitive mass sensor based on fiber can also be highly integrated for its small size, leading to a wider applied range of disciplines, spanning from biomechanical sensing to fundamental physics.

Funding. National Key Research and Development Program of China (2023YFB3209500); National Natural Science Foundation of China (62422511, 62374111); Shenzhen Science and Technology Program (Shenzhen Key Laboratory of Ultrafast Laser Micro/Nano Manufacturing) (ZDSYS20220606100405013); China Postdoctoral Science Foundation (2024T170579).

Disclosures. The authors declare no conflicts of interest.

Data Availability. Data underlying the results presented in this paper are not publicly available at this time but may be obtained from the authors upon reasonable request.

REFERENCES

1. F. F. Delgado, N. Cermak, V. C. Hecht, *et al.*, "Intracellular water exchange for measuring the dry mass, water mass and changes in chemical composition of living cells," PLOS ONE **8**, e67590 (2013).
2. M. Loferer-Krössbacher, J. Klima, and R. Psenner, "Determination of bacterial cell dry mass by transmission electron microscopy and densitometric image analysis," Appl. Environ. Microb. **64**, 688–694 (1998).
3. B. D. Chan, K. Icoz, W. F. Huang, *et al.*, "On-demand weighing of single dry biological particles over a 5-order-of-magnitude dynamic range," Lab Chip **14**, 4188–4196 (2014).
4. S. Faez, Y. Lahini, S. Weidlich, *et al.*, "Fast, label-free tracking of single viruses and weakly scattering nanoparticles in a nanofluidic optical fiber," ACS Nano **9**, 12349–12357 (2015).
5. O. Malvar, J. J. Ruz, P. M. Kosaka, *et al.*, "Mass and stiffness spectrometry of nanoparticles and whole intact bacteria by multimode nanomechanical resonators," Nat. Commun. **7**, 13452 (2016).
6. K. Jensen, K. Kim, and A. Zettl, "An atomic-resolution nanomechanical mass sensor," Nat. Nanotechnol. **3**, 533–537 (2008).
7. X. W. Lei, T. Natsuki, J. X. Shi, *et al.*, "An atomic-resolution nanomechanical mass sensor based on circular monolayer graphene sheet: theoretical analysis of vibrational properties," J. Appl. Phys. **113**, 154313 (2013).
8. A. Heck and J. Krijgsveld, "Mass spectrometry-based quantitative proteomics," Expert Rev. Proteomic. **1**, 317–326 (2004).
9. T. E. Angel, U. K. Aryal, S. M. Hengel, *et al.*, "Mass spectrometry-based proteomics: existing capabilities and future directions," Chem. Soc. Rev. **41**, 3912–3928 (2012).
10. Y. P. Chen, S. Liu, G. Q. Hong, *et al.*, "Nano-optomechanical resonators for sensitive pressure sensing," ACS Appl. Mater. Inter. **14**, 39211–39219 (2022).
11. R. J. Dolleman, D. Davidovikj, S. J. Cartamil-Bueno, *et al.*, "Graphene squeeze-film pressure sensors," Nano Lett. **16**, 568–571 (2016).
12. S. Liu, Y. P. Chen, H. L. Lai, *et al.*, "Room-temperature fiber tip nanoscale optomechanical bolometer," ACS Photonics **9**, 1586–1593 (2022).
13. A. Blaikie, D. Miller, and B. J. Alemán, "A fast and sensitive room-temperature graphene nanomechanical bolometer," Nat. Commun. **10**, 4726 (2019).
14. S. Liu, P. J. Chen, J. X. Luo, *et al.*, "Nano-optomechanical resonators based graphene/Au membrane for current sensing," J. Lightwave Technol. **40**, 7200–7207 (2022).
15. J. X. Luo, S. Liu, P. J. Chen, *et al.*, "Highly sensitive hydrogen sensor based on an optical driven nanofilm resonator," ACS Appl. Mater. Inter. **14**, 29357–29365 (2022).
16. D. Miller and B. Alemán, "Spatially resolved optical excitation of mechanical modes in graphene NEMS," Appl. Phys. Lett. **115**, 193102 (2019).
17. S. Stassi, I. Cooperstein, M. Tortello, *et al.*, "Reaching silicon-based NEMS performances with 3D printed nanomechanical resonators," Nat. Commun. **12**, 6080 (2021).
18. J. X. Luo, S. Liu, P. J. Chen, *et al.*, "Fiber optic hydrogen sensor based on a Fabry-Perot interferometer with a fiber Bragg grating and a nanofilm†," Lab Chip **21**, 1752–1758 (2021).
19. J. L. Zhong, S. Z. Lu, S. Liu, *et al.*, "Fiber-tip Fabry-Perot interferometer with a graphene-Au-Pd cantilever for trace hydrogen sensing," Lab Chip **23**, 3518–3526 (2023).
20. M. Q. Zou, C. R. Liao, S. Liu, *et al.*, "Fiber-tip polymer clamped-beam probe for high-sensitivity nanoforce measurements," Light Sci. Appl. **10**, 171 (2021).
21. F. M. Wang, M. Q. Zou, C. R. Liao, *et al.*, "Three-dimensional printed microcantilever with mechanical metamaterial for fiber-optic microforce sensing," APL Photonics **8**, 096108 (2023).
22. B. Z. Li, C. R. Liao, Z. H. Cai, *et al.*, "Femtosecond laser 3D printed micro objective lens for ultrathin fiber endoscope," Fundamental Research **4**, 123–130 (2024).
23. S. Lightman, O. Porat, G. Hurvitz, *et al.*, "Vortex-Bessel beam generation by 3D direct printing of an integrated multi-optical element on a fiber tip," Opt. Lett. **47**, 5248–5251 (2022).
24. Z. K. Chen, L. P. Wu, B. Z. Li, *et al.*, "Tunable Bessel beam generator based on a 3D-printed helical axicon on a fiber tip," Opt. Lett. **49**, 494–497 (2024).
25. S. Liu, Z. Y. Sun, L. Zhang, *et al.*, "Strain-based tunable optical microresonator with an in-fiber rectangular air bubble," Opt. Lett. **43**, 4077–4080 (2018).
26. W. Yu, J. J. Zhu, Y. Xu, *et al.*, "Optical nanofiber-enabled self-detection picobalance," ACS Photonics **11**, 2316–2323 (2024).
27. J. Ma, "Miniature fiber-tip Fabry-Perot interferometric sensors for pressure and acoustic detection," PhD Dissertation (Hong Kong Polytechnic University, 2014).
28. F. C. Zhang, X. Z. Xu, J. He, *et al.*, "Highly sensitive temperature sensor based on a polymer-infiltrated Mach-Zehnder interferometer created in graded index fiber," Opt. Lett. **44**, 2466–2469 (2019).
29. S. Liu, Y. P. Wang, C. R. Liao, *et al.*, "High-sensitivity strain sensor based on in-fiber improved Fabry-Perot interferometer," Opt. Lett. **39**, 2121–2124 (2014).
30. I. M. White and X. D. Fan, "On the performance quantification of resonant refractive index sensors," Opt. Express **16**, 1020–1028 (2008).
31. X. G. Shang, N. Wang, S. M. Cao, *et al.*, "Fiber-integrated force sensor using 3D printed spring-composed Fabry-Perot cavities with a high precision down to tens of piconewton," Adv. Mater. **36**, 2305121 (2024).